

Multi-Dress-State Engineered Rydberg Electrometry: Achieving 100-MHz-level Instantaneous-Bandwidth

Yuhan Yan^{1,2†}, Bowen Yang^{2†}, Xuejie Li^{1,2}, Haojie Zhao², Binghong Yu², Jianliao Deng^{2,3*},
L. Q. Chen^{1,4*}, Huadong Cheng^{2,3*}

¹State Key Laboratory of Precision Spectroscopy, Department of Physics and Electronic Science, East China Normal University, Shanghai, 200062, China.

²Wangzhijiang Innovation Center for Laser, Aerospace Laser Technology and System Department, Shanghai Institute of Optics and Fine Mechanics, Chinese Academy of Sciences, Shanghai, 201800, China.

³Center of Materials Science and Optoelectronics Engineering, University of Chinese Academy of Sciences, Beijing, 100049, China.

⁴Shanghai Branch, Hefei National Laboratory, Shanghai, 201315, China.

*Corresponding author(s). E-mail(s): jldeng@siom.ac.cn; lqchen@phy.ecnu.edu.cn; chenghd@siom.ac.cn;

†These authors contributed equally to this work.

Abstract

Rydberg atoms, with their giant electric dipole moments and tunable energy-level transitions, offer exceptional potential for microwave (MW) electric field sensing, combining high sensitivity and broad frequency coverage. However, simultaneously achieving high sensitivity and wide instantaneous bandwidth in a Rydberg-based MW transducer remains a critical challenge. Here, we propose a multi-dress-state engineered superheterodyne detection scheme for Rydberg electrometry that exploits a detuning-dependent dual-peak response structure and a Rabi-frequency-driven dip-lifting effect to overcome the limitation on instantaneous bandwidth. By strategically engineering the multiple dress states of Rydberg atoms, we demonstrate a thermal ⁸⁷Rb vapor-based transducer with a record sensitivity of $140.4 \text{ nV cm}^{-1} \text{ Hz}^{-1/2}$ and an instantaneous bandwidth of up to 54.6 MHz. The performance metrics are now approaching the practical requirements of modern MW receivers (100-MHz-level) in certain application fields. This advancement bridges the gap between atomic sensing and real-world applications, paving the way for Rydberg-atom technologies in radar, wireless communication, and spectrum monitoring.

Microwave (MW) detection plays a momentous role in the fields of cosmological research, radar technology and satellite communications¹⁻⁹. Rydberg atoms, characterized by their high major quantum numbers and large dipole moments, endow Rydberg MW sensors with significant advantages over traditional antennas, including a broad frequency response range, compact structural dimensions, and exceptional sensitivity¹⁰⁻¹⁶. These attributes have propelled Rydberg microwave detection technology to the forefront of high-sensitivity microwave measurement research. Sensitivity and instantaneous bandwidth (IB) are pivotal parameters in microwave measurement. Over the past decade, Rydberg MW transducers have achieved significant advancements in optimizing these two parameters independently¹⁷⁻³⁸. A Rydberg MW transducer with a sensitivity of $55 \text{ nV cm}^{-1} \text{ Hz}^{-1/2}$ and a 150 kHz IB using the superheterodyne method has been realized²². The sensitivity has been improved to $10 \text{ nV cm}^{-1} \text{ Hz}^{-1/2}$ with a wider IB of 4.6 MHz in a cold atom system³². The dual-beam excitation in a thermal cesium

vapor is utilized to enhance the IB and achieved a sensitivity of $468 \text{ nV cm}^{-1} \text{ Hz}^{-1/2}$ with 6.8 MHz IB³³. The NIST team demonstrated a 12 MHz IB with $1910 \text{ nV cm}^{-1} \text{ Hz}^{-1/2}$ sensitivity via frequency-comb probing^{34,35}. Notably, Bowen Yang et al. established the current record of $\pm 10.2 \text{ MHz}$ IB while maintaining $62 \text{ nV cm}^{-1} \text{ Hz}^{-1/2}$ sensitivity through dual-six-wave-mixing superheterodyne detection in a ⁸⁷Rb vapor³⁶.

For practical MW sensing applications (e.g., radar, 5G communications), the operational specifications require an IB of 100 MHz level while maintaining high sensitivity of $100 \text{ nV cm}^{-1} \text{ Hz}^{-1/2}$ level^{25,39,40}. While narrowband operation (MHz-level IB) with 10 nV-scale sensitivity has been demonstrated³², achieving 100-MHz-level IB detection with comparable sensitivity remains unrealized. This persistent gap in simultaneous high-sensitivity and broad-IB performance continues to pose fundamental technical challenges, necessitating novel methodological breakthroughs. In this article, we develop a multi-dress-state engineered superheterodyne (MDSSES) for Rydberg sensing system. IB is

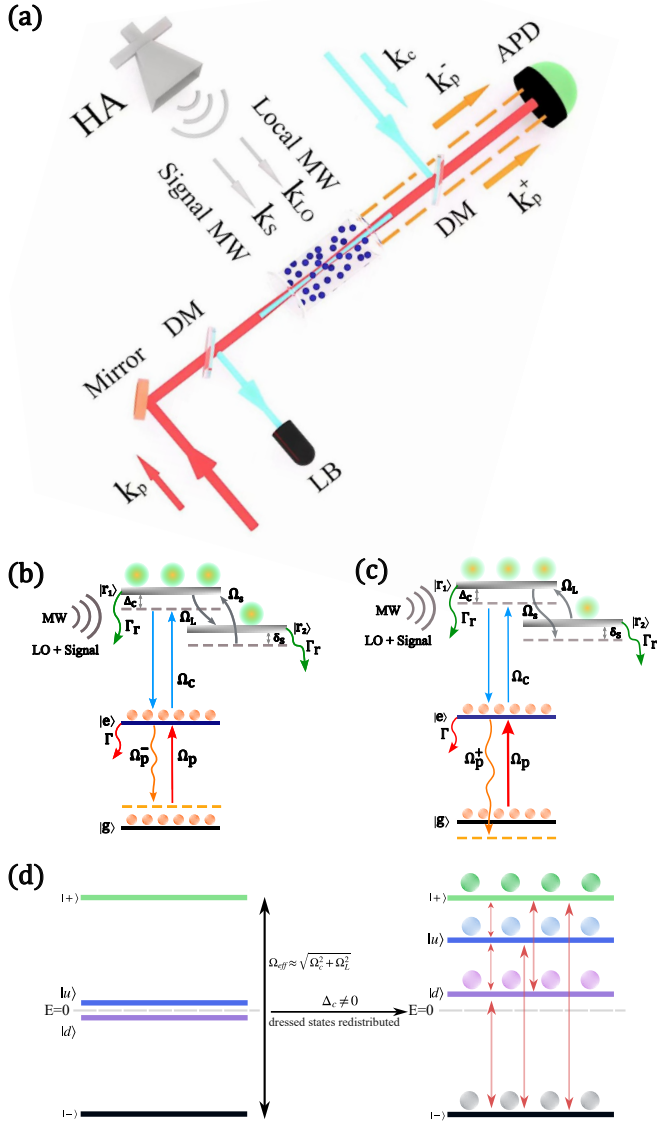


Fig. 1: The multi-dress-state engineering superheterodyne scheme. **(a)** Experimental setup. DM: dichroic mirror; LB: laser block; HA: horn antenna; APD: avalanche photodetector. Atomic energy levels for the negative sideband (NS in **(b)**) and positive sideband (PS in **(c)**). k_i, Ω_i, Δ_i : the wave vector, Rabi frequency and detuning frequency of the i field. $i = p, c, L, s$ represents the probe, coupling, local and signal MW fields, respectively. Superscript $+/-$ represents the PS and NS sidebands. $|g\rangle: |5S_{1/2}, F=2\rangle$; $|e\rangle: |5P_{3/2}, F'=3\rangle$; $|r_1\rangle: |51D_{5/2}, m_J=1/2\rangle$; $|r_2\rangle: |52P_{3/2}, m_J=1/2\rangle$. γt is the transient time broaden, Γ is the spontaneous decay rate of $|e\rangle$ and Γ_r is the spontaneous decay rate of $|r_1\rangle$ and $|r_2\rangle$. **(d)** The dressed states: $|-\rangle, |d\rangle, |u\rangle, |+\rangle$. Left is $\Delta_c = 0$ and right is $\Delta_c \neq 0$.

enhanced up to 54.6 MHz, approaching the practical demands of microwave antennas, while achieving superior sensitivity of $140.4 \text{ nV cm}^{-1} \text{ Hz}^{-1/2}$. The experimental configuration of MDSES with the corresponding energy level diagram is shown in Fig. 1. The core is an ^{87}Rb atomic vapor cell. The atoms at the ground state $|g\rangle$ are excited to the Rydberg state $|r_1\rangle$ by the probe field Ω_p and coupling field Ω_c . The probe field is resonant on the atomic transition $|g\rangle \rightarrow |e\rangle$. The probe

and coupling beams are counter-propagating, effectively cancelling out the Doppler effect on EIT. With the local (Ω_L) and signal (Ω_s) MW coupling the Rydberg states $|r_1\rangle$ and $|r_2\rangle$, two six-wave mixing processes are established simultaneously to generate the negative sideband Ω_p^- (NS, in Fig. 1(b)) with angular frequency $\omega_p^- = \omega_p - \delta_s$ and positive sideband Ω_p^+ (PS, in Fig. 1(c)) with angular frequency $\omega_p^+ = \omega_p + \delta_s$, where $\delta_s = \omega_s - \omega_L$ is the angular frequency difference of signal and local MW. Then, two sideband waves are mixing with the probe field Ω_p , forming a superheterodyne signal detected by the avalanche photodetector (APD). The intensity and frequency of superheterodyne signal is directly related to that of the signal MW field. Therefore, optimization of the superheterodyne response on signal MW via parameter engineering is the critical approach to improve sensitivity and IB. In the experiment, six key parameters predominantly govern the system's response to the signal MW field: the Rabi frequencies $\Omega_L, \Omega_c, \Omega_p$ and the detunings $\Delta_L, \Delta_c, \Delta_p$. In following measurement, the frequencies of probe and local MW fields are always resonant, and Rabi frequency of probe field is fixed at $\Omega_p/2\pi = 17.16 \text{ MHz}$. We optimize both the sensitivity and instantaneous bandwidth by dynamically adjusting the parameters Ω_L, Ω_c , and Δ_c .

The distinctive feature of the MDSES scheme is the active manipulation of multiple dressed states via applying a finite Δ_c . Here, Δ_c denotes the detuning of the coupling field from the $|e\rangle \rightarrow |r_1\rangle$ transition—serving as the key parameter for engineering multiple dressed states in superheterodyne detection. Below, we will theoretically analyze the impact of Δ_c on the dressed states, and then experimentally demonstrate the Δ_c -dependent system response, achieving both optimal sensitivity and enhanced IB.

First, we present the physical mechanism of MDSES, where enhanced IB emerges from dressed-state redistribution under non-zero coupling detuning ($\Delta_c \neq 0$). As shown in Fig. 1(d), driving by the strong coupling (Ω_c) and local microwave (Ω_L) fields, the atom-light interaction system generates four dressed states ($|-\rangle, |d\rangle, |u\rangle, |+\rangle$) via AC Stark effects. In the case of $\Delta_c = 0$, these states distribute symmetrically with energy splitting $\Delta E_{\pm} = \Omega_{eff} \approx \sqrt{\Omega_c^2 + \Omega_L^2}$, while $|E_d| = |E_u| \approx 0$. This creates symmetric resonance peaks at $\delta_s \approx \pm \sqrt{\Omega_c^2 + \Omega_L^2}/2$, where the largest IB of 10.2 MHz is achieved³⁶. The current MDSES protocol achieves record-breaking IB operation by employing finite coupling detuning ($\Delta_c \neq 0$). This detuning breaks dressed-state symmetry ($\Delta E_{\pm} \neq \Omega_{eff}$), causing unidirectional shifts of $|u\rangle$ and $|d\rangle$ states from zero energy that increase ΔE_{du} , with shift direction controlled by coupling detuning sign (Δ_c is red or blue detuning). Superheterodyne response reflects the coherence between the $|g\rangle$ and $|e\rangle$ states. Consequently, the response amplitude and IB are governed by the collective coherence across all dressed-state transition channels, causing response peaks to emerge at overall coherence maxima rather than dressed-state resonance conditions^{41, 42}. Dressed-state redistribution (Fig. 1d) enables coherence manipulation across a broad δ_s range for IB enhancement. Subsequent experiments identify coherence maxima conditions, enabling instantaneous bandwidth (IB) exceeding the 10 MHz state-of-the-art limit and achieving high-sensitivity simultaneously. In

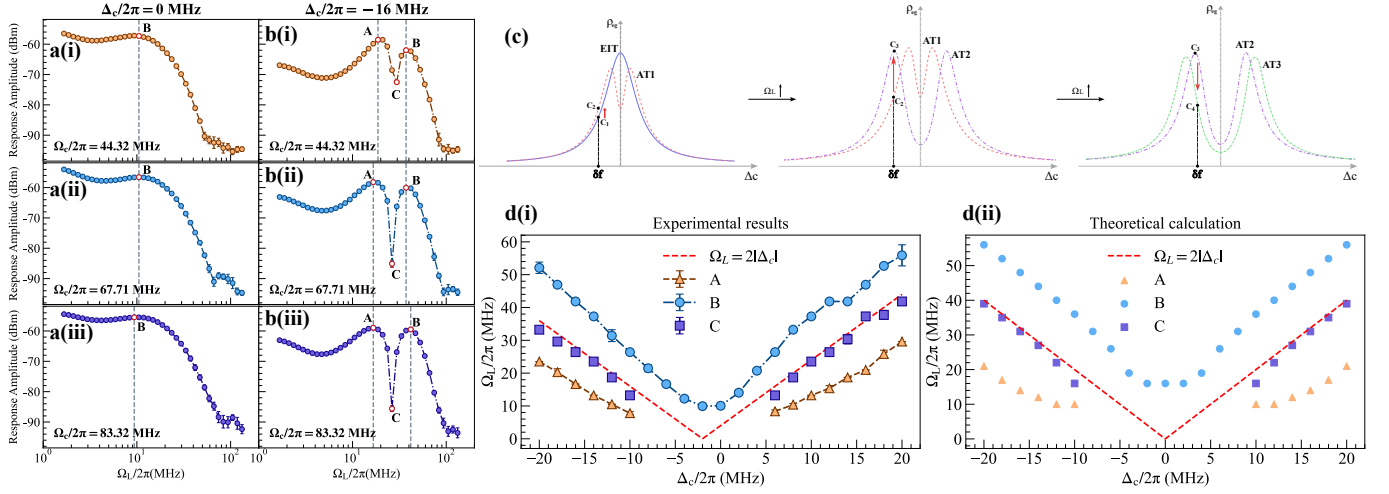


Fig. 2: The experimental results and physical mechanism for dual response peaks. The response amplitude as a function of Ω_L at $\Delta_c/2\pi = 0$ MHz in **a(i-iii)** and $\Delta_c/2\pi = -16$ MHz in **b(i-iii)**. **(c)** Physical mechanisms for dual response peaks A and B. AT: Autler-Townes splitting. EIT: electromagnetically induced transparency. Δ_c is fixed at δ_f detuning and Ω_L increase sequentially from left to right. **(d)** Ω_L as a function of Δ_c at response peaks A and B in experiment **(i)** and theory **(ii)**. The red dashed lines in **d(i, ii)** represent $\Omega_L = 2|\Delta_c|$, where the slope of Autler-Townes splitting is zero as shown in **(c)**. In all figures, the signal MW power is -45 dBm and the detuning frequency is $|\delta_s|/2\pi = 200$ kHz with $\Omega_p/2\pi = 17.16$ MHz. The error bar in **(a, b, d)** denotes the standard deviation of 10 measurements.

experiment, the Rydberg atomic sensor's microwave detection performance is optimized through two steps: the first is parametric optimization of probe, coupling and local MW fields to establish peak response conditions, then the second step is stabilizing these operational parameters, characterizing the frequency response to determine IB and achieving the sensitivity. The system initially finds the peak response conditions. Figure 2 shows the superheterodyne response's dependence on Rabi frequencies (Ω_L , Ω_c) under fixed Δ_c and δ_s . For resonant coupling ($\Delta_c = 0$ MHz, Fig. 2a), the response curves exhibit a single-peak characteristic with the increase of Ω_L : an initial gradual decrease, followed by a slow increase to maximum value, and ultimately a rapid decline. When $\Delta_c \neq 0$ MHz (Fig. 2b), the detuning frequency induces a bifurcation into two spectrally distinct peaks, denoted as peak A and peak B, whose physical origin is elucidated in Fig. 2c. When Δ_c is fixed at a detuning frequency δ_f ($\delta_f > \Omega_L/2$), progressive increase of Ω_L generates monotonically increasing Autler-Townes (AT) splitting, driving the superheterodyne signal amplitude through critical points C_1 - C_4 . The dual-peak structure emerges from slope extrema at C_2 (forming peak A) and C_4 (forming peak B), separated by a null-slope inflection at C_3 .

The $\Delta_c - \Omega_L$ correlation curves for peak A and B in Fig. 2d provide experimental confirmation of the dual-peak mechanism. In Figs. 2a-b, the response values of both peaks show a monotonic dependence on Ω_c , regardless of whether Δ_c equals zero. Therefore, we fix Ω_c at its maximum achievable value ($\Omega_c/2\pi = 83.32$ MHz), remain Δ_c at a specified value, and then scan Ω_L to obtain the spectral response profile. Through this procedure, the Ω_L values of response peaks A and B are achieved. The curves in Fig. 2d demonstrate two key features: a linear scaling of Ω_L with Δ_c for both A and B peaks, and consistently smaller Ω_L requirements for peak A compared to peak B. These experimental observations

agree with physical mechanism in Fig. 2c. As further demonstrated in Fig. 2d(i), the response peak A disappears when -10 MHz $< \Delta_c/2\pi < 6$ MHz, resulting in the emergence of a single peak B. The Rabi frequencies $\Omega_L/2\pi = 7.8$ MHz at $\Delta_c/2\pi = -10$ MHz and 8.36 MHz at $\Delta_c/2\pi = 6$ MHz are approximately equal to $\Gamma_{EIT}/2 = 8.63$ MHz, which means that peak A only appears when existing a certain detuning Δ_c and $\Omega_L > \Gamma_{EIT}/2$. This point matches the theoretical analysis well (Fig. 2d(ii)). Furthermore, the behavior that peak A vanishes for $\Delta_c \in (-10, 6)$ MHz can be explained physically from Fig. 2c. When $\Delta_c = \delta_f$ is operated at near resonance, the system only experiences C_4 during Ω_L increases, producing a single response maximum at C_4 instead of the dual-peak structure observed at large detunings $\Delta_c > \Gamma_{EIT}/2$.

The instantaneous bandwidth is characterized via the δ_s -dependent response of the system, measured under fixed $\Delta_c/2\pi = -16$ MHz and Ω_L at the peak A and B positions. Figures 3a(i, ii) displays the response for peak A as an example, revealing two key features. First, the response amplitude grows monotonically with Ω_c , attaining its maximum value at the strongest driving strength $\Omega_c/2\pi = 83.32$ MHz (consistent with Fig. 2b). Second, the response exhibits asymmetric patterns at the $\delta_s > 0$ and $\delta_s < 0$ regimes due to the multi-dress-state engineering. Crucially, there is a response dip at $\delta_s > 0$ region in Fig. 3a(ii), which significantly limits the instantaneous bandwidth. The instantaneous bandwidth is defined as the 3 dB bandwidth measured relative to the response amplitude at $\delta_s/2\pi = 200$ kHz. (as marked by the dashed line in the Fig. 3a). However, this dip lifts with increasing Ω_c values. When $\Omega_c/2\pi$ increases from 44.32 MHz to 83.32 MHz, the response amplitude of the dip rises by 6.8 dB, dramatically enhancing the IB from 1.6 MHz to 31.2 MHz, resulting in an approximate 20-fold broadening. Specifically, for $\delta_s < 0$, the instantaneous bandwidth is 7.6 MHz for $\Omega_c/2\pi = 44.32$ MHz, and is enhanced to 20.4 MHz and 23.4 MHz when $\Omega_c/2\pi$

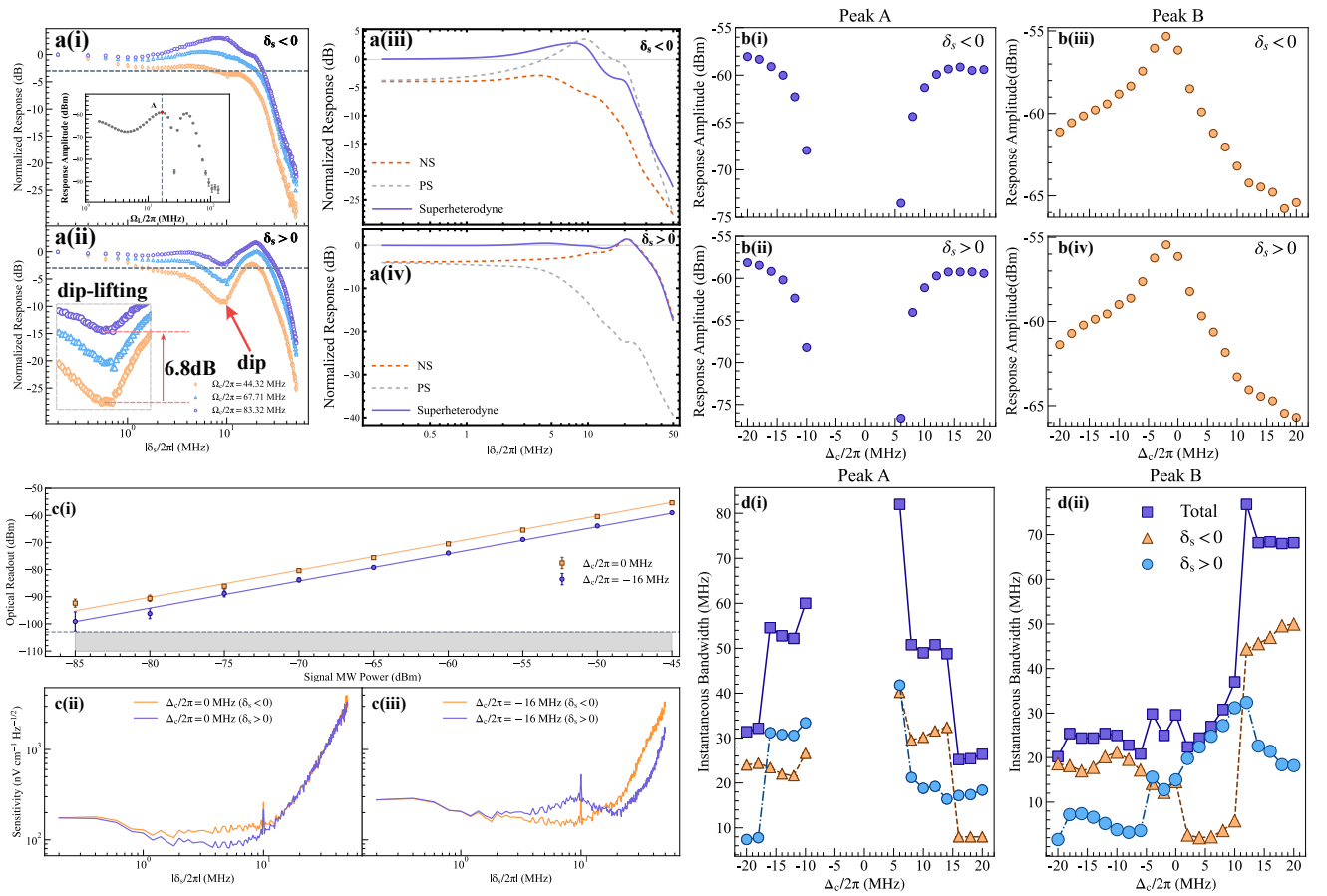


Fig. 3: Experimental results of sensitivity and instantaneous bandwidth. **a(i-ii)** The experimental normalized responses as a function of the signal MW frequency detuning δ_s . Ω_L fixed at the maximum response conditions of peak A and $\Omega_p/2\pi = 17.16$ MHz. The experimental data was measured at $\Delta_c/2\pi = -16$ MHz when $\Omega_c/2\pi = 44.32$ MHz (orange diamonds), 67.71 MHz (blue triangles) and 83.32 MHz (purple circles) for $\delta_s < 0$ (i) and $\delta_s > 0$ (ii). The gray dashed line represents the 3 dB attenuation in response amplitude. The signal MW power was maintained at -45 dBm. The inset in **a(i)** is the response amplitude of $|\delta_s|/2\pi = 200$ kHz at $\Delta_c/2\pi = -16$ MHz as a function of Ω_L with $\Omega_p/2\pi = 17.16$ MHz and $\Omega_c/2\pi = 83.32$ MHz. **a(iii-iv)** The theoretical normalized frequency responses of $\Omega_c/2\pi = 83.32$ MHz at $\Delta_c/2\pi = -16$ MHz for $\delta_s < 0$ (iii) and $\delta_s > 0$ (iv). **(b)** The response amplitude at different Δ_c for peak A (i-ii) and B (iii-iv) at $|\delta_s|/2\pi = 200$ kHz. **(c)** Sensitivity of the Rydberg MW transducer at $\Delta_c = 0$ MHz and $\Delta_c/2\pi = -16$ MHz. Optical readout of superheterodyne using a spectrum analyzer as a function of the signal MW power are shown in **c(i)**. The error bar denotes the standard deviation of measurement during 10 s in the zero span mode of the spectrum analyzer and the resolution bandwidth is set to 1 Hz. The solid lines are the linear fitting of the experimental data. The grey dashed line represents the noise floor of the system without signal MW. The noise limited sensitivity for $\Delta_c = 0$ MHz and $\Delta_c/2\pi = -16$ MHz are shown in (ii) and (iii). The mutation point, occurring at $|\delta_s|/2\pi = 10$ MHz, originates from the 10 MHz crystal oscillator, which serves as the reference signal for synchronizing the spectrum analyzer and signal generators. **(d)** The instantaneous bandwidth as a function of Δ_c . The figures (i) and (ii) represent the peak A and B, respectively. All the data was measured when $\Omega_p/2\pi = 17.16$ MHz and $\Omega_c/2\pi = 83.32$ MHz.

increases to 67.71 MHz and 83.32 MHz respectively. Thus, the Ω_c -driven lifting of the dip plays a crucial role for IB enhancement.

In Figs. 3a(iii, iv), we present corresponding theoretical analyses to show the physical origin for the dip-lifting phenomenon. The dashed and dotted curves correspond to the positive (PS) and negative (NS) sidebands, respectively, generated via two distinct six-wave mixing processes (Figs. 1b-c). A striking sign-dependent asymmetry emerges: PS dominates the superheterodyne signal for $\delta_s < 0$, while NS governs the response when $\delta_s > 0$. Crucially, the amplitude asymmetry between the NS and PS sidebands shows strong

dependence on both Δ_c and Ω_L , enabling dip-depth control through Δ_c tuning. This tunability originates from the Δ_c -dependent six-wave mixing processes.

Figure 3b presents the response amplitudes at $|\delta_s|/2\pi = 200$ kHz as a function of the detuning Δ_c at peak A and B, which exhibit fundamentally distinct behaviors. As Δ_c is varied from the detuned to resonant regime, the response value at peak A monotonically decreases, while peak B displays resonant enhancement. The optimal response for peak B occurs at a minimal detuning ($\Delta_c/2\pi = -2$ MHz), whereas peak A requires a significantly larger detuning ($\Delta_c/2\pi \sim 20$ MHz). To evaluate the performance of the Rydberg MW transducer, it is essential to determine the sensitivity by combining the response amplitude with the system noise characteristics. The

optical readout signal at $|\delta_s|/2\pi = 200$ kHz as a function of the signal MW power is shown in Fig. 3c(i), demonstrating excellent linear correlation. The sensitivity is characterized by the minimum detectable power that yields a unity signal-to-noise ratio (SNR = 1) in the optical readout signal. Figure 3c(i) presents the calibration method converting the minimum detectable power (unit: dBm) into noise limited sensitivity data (unit: $\text{nV cm}^{-1} \text{Hz}^{-1/2}$), establishing a conversion factor of $0.76 \text{ V m}^{-1} \text{mW}^{-1/2}$. Therefore, the electric amplitude of the applied signal MW field and the noise limited sensitivity can be deduced. The optimal sensitivities of peak B achieves $81.1 \text{ nV cm}^{-1} \text{Hz}^{-1/2}$ at zero detuning $\Delta_c/2\pi = 0$ MHz, whereas peak A attains $140.4 \text{ nV cm}^{-1} \text{Hz}^{-1/2}$ at $\Delta_c/2\pi = -16$ MHz with only minimal sensitivity degradation as shown in Fig. 3c(iii).

The data presented in Fig. 3b and Fig. 3d indicate an inverse relationship between response amplitude and instantaneous bandwidth. For peak A depicted in Fig. 3d(i), a systematic investigation demonstrates: (1) At a detuning of $\Delta_c/2\pi = -16$ MHz, the IB reaches 54.6 MHz with an optimal sensitivity of $140.4 \text{ nV cm}^{-1} \text{Hz}^{-1/2}$; (2) When $\Delta_c/2\pi = -10$ MHz, IB further increases to ~ 60 MHz, accompanied by a rapid decline in response magnitude while maintaining detectable sensitivity; (3) The maximum IB value of 82 MHz occurs at $\Delta_c/2\pi = 6$ MHz, though this operational point exhibits reduced response amplitude with corresponding sensitivity degradation to $1.25 \mu\text{V cm}^{-1} \text{Hz}^{-1/2}$. Regarding peak B as depicted in Fig. 3d(ii), the system's optimal performance is achieved at a detuning of $\Delta_c/2\pi = 12$ MHz, where the IB reaches 76.8 MHz with an optimum sensitivity of $222.6 \text{ nV cm}^{-1} \text{Hz}^{-1/2}$.

The experimental results confirm that the IB values of 82 MHz for peak A and 76.8 MHz for peak B are attainable, although this is accompanied by a certain degree of sensitivity reduction. The globally optimal condition for peak A is found at $\Delta_c/2\pi = -16$ MHz, yielding an IB of 54.6 MHz with a sensitivity of $140.4 \text{ nV cm}^{-1} \text{Hz}^{-1/2}$.

Discussion

We have developed a broadband Rydberg microwave sensing method based on multi-dressed-state manipulation, achieving two groundbreaking observations: a novel dual-peak configuration and the dip-lifting effect. This approach simultaneously achieves 54.6 MHz instantaneous bandwidth while maintaining $140.4 \text{ nV}^{-1} \text{cm}^{-1} \text{Hz}^{-1/2}$ sensitivity - a performance envelope previously unachievable in resonant measurement schemes. The key innovation lies in Δ_c -induced dual response peaks, followed by strategic dip lifting that circumvents the fundamental IB limitations of single-peak systems.

Current scheme has three advances. First, the observed dual-peak configuration (absent in prior studies) enables new degrees of freedom for response shaping. Second, the dip-lifting effect provides a previously unavailable knob for IB enhancement without sensitivity trade-offs. Third, current IB reaching practical antenna requirements resolves a critical roadblock in Rydberg receiver development.

Further improvement of the IB and sensitivity can be realized by incorporating additional dressed parameters into the system. Crucially, this technique's architecture-agnostic nature makes it readily transferable to other Rydberg detection schemes, from superheterodyne to direct detection. Our results establish a universal pathway toward deployable Rydberg microwave sensors. The dressing-based control paradigm demonstrated here may find broader applications in quantum-enhanced metrology, particularly for other atomic systems where dynamic Stark effects can be similarly engineered.

Methods

Experimental setup. The atoms of a thermal ^{87}Rb vapor are excited from a ground state $|g\rangle = |5S_{1/2}, F = 2\rangle$ to a Rydberg state $|r_1\rangle = |51D_{5/2}, m_J = 1/2\rangle$ by two-photon cascade excitation scheme. The modulation transfer spectroscopy is used to stabilize the frequency of the probe laser which is continuously driving the atomic transition $|5S_{1/2}, F = 2\rangle$ to $|5P_{3/2}, F' = 3\rangle$, and the coupling laser is locked to a high-finesse Fabry-Perot cavity exciting the atoms to $|r_1\rangle = |51D_{5/2}, m_J = 1/2\rangle$ continuously. The probe and coupling lights are propagating in opposite directions to eliminate the Doppler effect. The waist radius of the probe and coupling beam are approximately $52.5 \mu\text{m}$ and $29 \mu\text{m}$, respectively. The local MW (generated from Ceyear 1465D signal generator with a frequency of 16.029985 GHz) and signal MW (generated from Agilent E8257D signal generator) coupling Rydberg state $|r_1\rangle = |51D_{5/2}, m_J = 1/2\rangle$ and $|r_2\rangle = |52P_{3/2}, m_J = 1/2\rangle$ are combined using a power combiner and emitted from a horn antenna to free space. All the fields are vertical polarized. To ensure the uniformity of MW, the horn antenna is positioned at a distance exceeding 50 cm from the atom cell. Furthermore, the cell is shielded by the microwave anechoic absorbers to mitigate reflections from conductors which might otherwise influence the measurement outcomes. The superheterodyne signal is detected by an avalanche photodetector (Thorlabs APD130A) and finally acquired by a spectrum analyzer (Keysight N9020A).

Multi-dress-state engineered superheterodyne (MDES).

The interaction between the electromagnetic fields and the four-level atomic system generates four dressed states ($|-\rangle$, $|d\rangle$, $|u\rangle$, $|+\rangle$). In the case of $\Delta_c = 0$, the four dressed states are symmetrically distributed, $|E_d\rangle = |E_u\rangle \approx 0$, and the energy difference between states $|-\rangle$ and $|+\rangle$ (ΔE_{\pm}) is approximately equal to $\Omega_{eff} = \sqrt{\Omega_c^2 + \Omega_L^2}$ with $|E_+\rangle = |E_-\rangle \approx \Omega_{eff}/2$. This causes the symmetric response peaks at $\delta_s = \pm\Omega_{eff}/2$. (Details in the Supplementary Materials.) However, when $\Delta_c \neq 0$, the dressed-state symmetry is broken ($|E_d\rangle \neq |E_u\rangle$, $|E_+\rangle \neq |E_-\rangle$, $\Delta E_{\pm} \neq \Omega_{eff}$). The shift direction of the dressed-state eigenenergies is governed by the detuning of the coupling light. The bare states ($|g\rangle$, $|e\rangle$, $|r_1\rangle$, $|r_2\rangle$) and dressed states ($|-\rangle$, $|d\rangle$, $|u\rangle$, $|+\rangle$) are related through a transformation matrix \mathcal{U} which can be written as

$\psi_B = U\psi_D$, where ψ_B and ψ_D are given as

$$\psi_B = \begin{pmatrix} |g\rangle \\ |e\rangle \\ |r_1\rangle \\ |r_2\rangle \end{pmatrix}, \psi_D = \begin{pmatrix} |- \rangle \\ |d\rangle \\ |u\rangle \\ |+\rangle \end{pmatrix} \quad (1)$$

Therefore, the signal MW part of the Hamiltonian in the dressed-state picture is

$$\begin{aligned} \hat{H}_S &= \frac{1}{2}(\Omega_s^* e^{-i\delta_s t} \hat{\sigma}_{r_1 r_2} + h.c.) \\ &= \frac{1}{2} \left(\Omega_s^* e^{-i\delta_s t} \sum_{i,j} D_{ij}^{r_1 r_2} + h.c. \right) \end{aligned} \quad (2)$$

where $D_{ij}^{r_1 r_2} = U_{r_1 i} U_{r_2 j}^*$ ($i, j \in \{-, d, u, +\}$). According to Eq. (2), we observe that the signal microwave field affects the dressed states through two distinct mechanisms: when $i = j$, it induces a periodic modulation of the eigenenergies of the dressed states; when $i \neq j$, it drives atomic transitions between different dressed states. Therefore, $D_{ij}^{r_1 r_2}$ acquires a well-defined physical interpretation. When $i = j$, $D_{ij}^{r_1 r_2}$ is directly related to the dressed-state energies; when $i \neq j$, $D_{ij}^{r_1 r_2}$ characterizes the coupling strength between different dressed states. The parameter $D_{ij}^{r_1 r_2}$ serves as a quantitative indicator that partially characterizes the key features of the response curves. According to the theory model of six wave mixing in the Supplementary Materials, the response amplitude of the MDSES is

$$\begin{aligned} S(\delta_s) &\propto \left| \rho_{ge,+1}^{(B)} - \rho_{ge,-1}^{(B)*} \right| \\ &= \left| \sum_{i,j} D_{ij}^{ge} \left(\rho_{ij,+1}^{(D)} - \rho_{ij,-1}^{(D)*} \right) \right| \end{aligned} \quad (3)$$

where $D_{ij}^{ge} = U_{gi} U_{ej}^*$ ($i, j \in \{-, d, u, +\}$). Equation (3) indicates that the response amplitude is related to the coupling strength and coherence between different dressed-state transitions. Therefore, a new methodology to improve the performance of superheterodyne signal is through manipulating the coupling strength and the overall coherence across all six dressed-state transition channels.

The details of the MDSES methods and physical analysis are illustrated in the Supplementary Materials.

Data availability

The data are available from the corresponding authors on reasonable request. Source data are provided with this paper.

Code availability

The codes are available from the corresponding authors upon reasonable request.

References

[1] Liddle, A. *An introduction to modern cosmology* (John Wiley & Sons, 2015).

- [2] Durrer, R. The cosmic microwave background: the history of its experimental investigation and its significance for cosmology. *Classical Quantum Gravity* **32**, 124007 (2015).
- [3] Skolnik, M. Role of radar in microwaves. *IEEE Trans. Microwave Theory Tech.* **50**, 625–632 (2002).
- [4] Pan, S. & Zhang, Y. Microwave photonic radars. *J. Lightwave Technol.* **38**, 5450–5484 (2020).
- [5] Sobol, H. Microwave communications—an historical perspective. *IEEE Trans. Microwave Theory Tech.* **32**, 1170–1181 (1984).
- [6] Tsui, J. B. & Stephens, J. P. Digital microwave receiver technology. *IEEE Trans. Microwave Theory Tech.* **50**, 699–705 (2002).
- [7] Fan, H. *et al.* Atom based RF electric field sensing. *J. Phys. B:At., Mol. Opt. Phys.* **48**, 202001 (2015).
- [8] Yuan, J. *et al.* Quantum sensing of microwave electric fields based on Rydberg atoms. *Rep. Prog. Phys.* (2023).
- [9] Schlossberger, N. *et al.* Rydberg states of alkali atoms in atomic vapour as si-traceable field probes and communications receivers. *Nat. Rev. Phys.* 1–15 (2024).
- [10] Saffman, M., Walker, T. G. & Mølmer, K. Quantum information with Rydberg atoms. *Rev. Mod. Phys.* **82**, 2313–2363 (2010).
- [11] Holloway, C. L. *et al.* Broadband Rydberg atom-based electric-field probe for si-traceable, self-calibrated measurements. *IEEE Trans. Antennas Propag.* **62**, 6169–6182 (2014).
- [12] Holloway, C. L. *et al.* Atom-based RF electric field metrology: from self-calibrated measurements to sub-wavelength and near-field imaging. *IEEE Trans. Electromagn. Compat.* **59**, 717–728 (2017).
- [13] Holloway, C. L. *et al.* Electric field metrology for si traceability: Systematic measurement uncertainties in electromagnetically induced transparency in atomic vapor. *J. Appl. Phys.* **121** (2017).
- [14] Anderson, D. A., Sapiro, R. E. & Raitchel, G. Rydberg atoms for radio-frequency communications and sensing: Atomic receivers for pulsed RF field and phase detection. *IEEE Aerosp. Electron. Syst. Mag.* **35**, 48–56 (2020).
- [15] Meyer, D. H., Castillo, Z. A., Cox, K. C. & Kunz, P. D. Assessment of Rydberg atoms for wideband electric field sensing. *J. Phys. B:At., Mol. Opt. Phys.* **53**, 034001 (2020).
- [16] Meyer, D. H., Kunz, P. D. & Cox, K. C. Waveguide-coupled Rydberg spectrum analyzer from 0 to 20 ghz. *Phys. Rev. Appl.* **15**, 014053 (2021).

- [17] Sedlacek, J. A. *et al.* Microwave electrometry with Rydberg atoms in a vapour cell using bright atomic resonances. *Nat. Phys.* **8**, 819–824 (2012).
- [18] Sedlacek, J., Schwettmann, A., Kübler, H. & Shaffer, J. Atom-based vector microwave electrometry using rubidium Rydberg atoms in a vapor cell. *Phys. Rev. Lett.* **111**, 063001 (2013).
- [19] Anderson, D. *et al.* Two-photon microwave transitions and strong-field effects in a room-temperature Rydberg-atom gas. *Phys. Rev. A* **90**, 043419 (2014).
- [20] Miller, S. A., Anderson, D. A. & Raithel, G. Radio-frequency-modulated Rydberg states in a vapor cell. *New J. Phys.* **18**, 053017 (2016).
- [21] Anderson, D. A. *et al.* Optical measurements of strong microwave fields with Rydberg atoms in a vapor cell. *Phys. Rev. Appl.* **5**, 034003 (2016).
- [22] Jing, M. *et al.* Atomic superheterodyne receiver based on microwave-dressed Rydberg spectroscopy. *Nat. Phys.* **16**, 911–915 (2020).
- [23] Prajapati, N. *et al.* Enhancement of electromagnetically induced transparency based Rydberg-atom electrometry through population repumping. *Appl. Phys. Lett.* **119** (2021).
- [24] Liu, X.-H. *et al.* Continuous-frequency microwave heterodyne detection in an atomic vapor cell. *Phys. Rev. Appl.* **18**, 054003 (2022).
- [25] Zhang, L.-H. *et al.* Rydberg microwave-frequency-comb spectrometer. *Phys. Rev. Appl.* **18**, 014033 (2022).
- [26] Liu, Z.-K. *et al.* Deep learning enhanced Rydberg multifrequency microwave recognition. *Nat. Commun.* **13**, 1997 (2022).
- [27] Ding, D.-S. *et al.* Enhanced metrology at the critical point of a many-body Rydberg atomic system. *Nat. Phys.* **18**, 1447–1452 (2022).
- [28] Tu, H.-T. *et al.* High-efficiency coherent microwave-to-optics conversion via off-resonant scattering. *Nat. Photonics* **16**, 291–296 (2022).
- [29] Ouyang, K., Shi, Y., Lei, M. & Shi, M. Continuous broadband microwave electric field measurement in Rydberg atoms based on the DC stark effect. *Appl. Phys. Lett.* **123** (2023).
- [30] Berweger, S. *et al.* Closed-loop quantum interferometry for phase-resolved Rydberg-atom field sensing. *Phys. Rev. Appl.* **20**, 054009 (2023).
- [31] Borówka, S., Pylypenko, U., Mazelanik, M. & Parniak, M. Continuous wideband microwave-to-optical converter based on room-temperature Rydberg atoms. *Nat. Photonics* **18**, 32–38 (2024).
- [32] Tu, H.-T. *et al.* Approaching the standard quantum limit of a Rydberg-atom microwave electrometer. *Sci. Adv.* **10**, eads0683 (2024).
- [33] Hu, J. *et al.* Improvement of response bandwidth and sensitivity of Rydberg receiver using multi-channel excitations. *EPJ QUANTUM TECHNOL* **10**, 51 (2023).
- [34] Dixon, K., Nickerson, K., Booth, D. W. & Shaffer, J. P. Rydberg-atom-based electrometry using a self-heterodyne frequency-comb readout and preparation scheme. *Phys. Rev. Appl.* **19**, 034078 (2023).
- [35] Artusio-Glimpse, A. B. *et al.* Increased instantaneous bandwidth of Rydberg atom electrometry with an optical frequency comb probe. *arXiv preprint arXiv:2402.17942* (2024).
- [36] Yang, B. *et al.* Highly sensitive microwave electrometry with enhanced instantaneous bandwidth. *Phys. Rev. Appl.* **21**, L031003 (2024).
- [37] Wu, K.-D. *et al.* Nonlinearity-enhanced continuous microwave detection based on stochastic resonance. *Sci. Adv.* **10**, eado8130 (2024).
- [38] Cloutman, M. *et al.* Polarization-insensitive microwave electrometry using Rydberg atoms. *Phys. Rev. Appl.* **21**, 044025 (2024).
- [39] Bohaichuk, S. M., Booth, D., Nickerson, K., Tai, H. & Shaffer, J. P. Origins of Rydberg-atom electrometer transient response and its impact on radio-frequency pulse sensing. *Phys. Rev. Appl.* **18**, 034030 (2022).
- [40] Knarr, S. H. *et al.* Spatiotemporal multiplexed Rydberg receiver. *IEEE Transactions on Quantum Engineering* **4**, 1–8 (2023).
- [41] Bracht, T. K. *et al.* Dressed-state analysis of two-color excitation schemes. *Phys. Rev. B* **107**, 035425 (2023).
- [42] Li, J.-y. & Yang, Y. Resonant fluorescence of a bichromatically driven three-level atom with the electron shelving effect. *Phys. Rev. A* **110**, 053708 (2024).

Acknowledgements

Thanks for financially supported by the National Key Research and Development Program of China (2024YFA1409404), the National Natural Science Foundation of China (Grants No. 12174409, No. 12304294, No. U23A2075, and No. 12274132), the Fundamental Research Funds for the Central Universities and Shanghai Municipal Education Commission (202101070008E00099).

Author contributions

Y. Y. and B.Y. demonstrated the experimental setup and observed the phenomena, performed the measurements and analyzed data. All other authors discussed experimental results. The theoretical analysis and numerical simulations

are conducted by Y. Y and B. Y. X. L., H. Z. and B. Y. gave crucial assistance for collecting data. The manuscript was written by Y. Y. All authors discussed and contributed to the manuscript. J. D. , L. C. and H. C. supervised the study and suggested the writing of the manuscript.

Competing interests

The authors declare no competing interests.

Additional information

Supplementary information. Physical analysis, theoretical calculations, and the details of the experiment.

Supplementary Text

Supplementary Equations (S1-S32)

Supplementary Figures 1-8

Supplementary Table 1

References 1-5